

Article

# Effects of the Interface between Inorganic and Organic Components in a Bi<sub>2</sub>Te<sub>3</sub>–Polypyrrole Bulk Composite on Its Thermoelectric Performance

Cham Kim <sup>1,\*</sup> and David Humberto Lopez <sup>2</sup> 

<sup>1</sup> Division of Nanotechnology, Daegu Gyeongbuk Institute of Science and Technology (DGIST), 333 Techno Jungang-daero, Daegu 42988, Korea

<sup>2</sup> Department of Chemical and Environmental Engineering, University of Arizona, 1133 E. James. E. Rogers Way, Tucson, AZ 85721, USA; davidlopez3@email.arizona.edu

\* Correspondence: charming0207@dgist.ac.kr

**Abstract:** We provided a method to hybridize Bi<sub>2</sub>Te<sub>3</sub> with polypyrrole, thus forming an inorganic/organic bulk composite (Bi<sub>2</sub>Te<sub>3</sub>–polypyrrole), in which the effects of energy band junction and phonon scattering were expected to occur at the interface of the two components. Bi<sub>2</sub>Te<sub>3</sub>–polypyrrole exhibited a considerably high Seebeck coefficient compared to pristine Bi<sub>2</sub>Te<sub>3</sub>, and thus it recorded a somewhat increased power factor despite the loss in electrical conductivity caused by the organic component, polypyrrole. Bi<sub>2</sub>Te<sub>3</sub>–polypyrrole also exhibited much lower thermal conductivity than pristine Bi<sub>2</sub>Te<sub>3</sub> because of the phonon scattering effect at the interface. We successfully brought about the decoupling phenomenon of electrical and thermal properties by devising an inorganic/organic composite and adjusting its fabrication condition, thereby optimizing its thermoelectric performance, which is considered the predominant property for n-type binary Bi<sub>2</sub>Te<sub>3</sub> reported so far.

**Keywords:** thermoelectric material; Bi<sub>2</sub>Te<sub>3</sub>; polypyrrole; composite; interface



**Citation:** Kim, C.; Lopez, D.H. Effects of the Interface between Inorganic and Organic Components in a Bi<sub>2</sub>Te<sub>3</sub>–Polypyrrole Bulk Composite on Its Thermoelectric Performance. *Materials* **2021**, *14*, 3080. <https://doi.org/10.3390/ma14113080>

Academic Editor: Jong-Soo Rhyee

Received: 29 April 2021

Accepted: 31 May 2021

Published: 4 June 2021

**Publisher's Note:** MDPI stays neutral with regard to jurisdictional claims in published maps and institutional affiliations.



**Copyright:** © 2021 by the authors. Licensee MDPI, Basel, Switzerland. This article is an open access article distributed under the terms and conditions of the Creative Commons Attribution (CC BY) license (<https://creativecommons.org/licenses/by/4.0/>).

## 1. Introduction

The overall performance of thermoelectric materials is generally estimated via the dimensionless figure of merit,  $ZT$  ( $=\alpha^2\sigma T/\kappa$ ,  $\alpha$ : Seebeck coefficient,  $\sigma$ : electrical conductivity,  $\kappa$ : the thermal conductivity,  $T$ : absolute temperature) [1–3]. A high  $ZT$  value can be achieved by increasing the electrical property—that is, the power factor ( $\alpha^2\sigma$ )—and by decreasing the thermal conductivity [4–6]. Many researchers have endeavored to decouple the electrical and thermal properties of diverse materials by devising nanostructures [7–9], by introducing nano-inclusions [10–12], and by injecting metallic or nonmetallic atoms [13–15], which were shown to increase the power factor and/or decrease the thermal conductivity. Conducting polymers are recognized as promising candidates for thermoelectric applications because of their low thermal conductivity and moderate electrical conductivity as thermoelectric materials [16–18]. These polymers are often offered as flexible thin films, which are easily applicable to micro energy-harvesting devices for low-temperature thermoelectric operations. Many researchers have attempted to hybridize conducting polymers with inorganic Bi<sub>2</sub>Te<sub>3</sub> for low-temperature operations [19–21], as they expected to achieve low thermal conductivity due to conducting polymers and supplement electrical conductivity via inorganic Bi<sub>2</sub>Te<sub>3</sub>. However, these hybrid materials exhibited poorer electrical properties than inorganic Bi<sub>2</sub>Te<sub>3</sub> alone, possibly due to the low carrier transport properties of conducting polymers or severe carrier scattering at the component interfaces. In the present work, we tried to decrease the possible loss in electrical properties by hybridizing inorganic Bi<sub>2</sub>Te<sub>3</sub> with a conducting polymer (polypyrrole) and regulating the fabrication process to obtain an optimized bulk structure. We developed a brief fabrication process, in which a small amount of polypyrrole was dispersed in n-type Bi<sub>2</sub>Te<sub>3</sub>, and the resulting composite was packed via spark plasma sintering under different conditions; thus, we

gained an optimized composite material in the bulk phase. The composite inevitably showed inferior electrical conductivity than pristine  $\text{Bi}_2\text{Te}_3$  because of carrier scattering and carrier offsetting at the interfaces of the components, resulting in reductions in carrier mobility and carrier concentration, respectively. However, the composite recorded an improved Seebeck coefficient compared to pristine  $\text{Bi}_2\text{Te}_3$  due to the decrease in the carrier concentration, thus providing a somewhat increased power factor. Due to possible phonon scattering at the interface, in addition to the reduced carrier mobility and concentration, the composite exhibited lower thermal conductivity than pristine  $\text{Bi}_2\text{Te}_3$ . The electrical and thermal properties were successfully decoupled and optimized, and thus, the composite material provided significantly enhanced thermoelectric performance, which is considered a predominant property for n-type binary  $\text{Bi}_2\text{Te}_3$  reported so far.

## 2. Materials and Methods

### 2.1. Chemicals

Bismuth (99.99%, Vital Materials, Guangzhou, China) and tellurium granules (99.9%, Vital Materials, Guangzhou, China) with pyrrole (98%, Sigma-Aldrich, St. Louis, MO, USA) were used as raw materials. Chemical oxidation of pyrrole was conducted by using Iron(III) sulfate (97%, Sigma-Aldrich, St. Louis, MO, USA). Each chemical was used with no further purification.

### 2.2. Sample Preparation

Sample preparations were performed through our procedures described elsewhere [22].  $\text{Bi}_2\text{Te}_3$  powder was prepared by a conventional pulverization method. Proper stoichiometric amounts of the raw metal elements (Bi and Te granules) for the  $\text{Bi}_2\text{Te}_3$  composite were weighed out and placed in a quartz tube, which was then evacuated and sealed. The tube was installed in a rocking furnace and heated to 900 °C ( $9\text{ °C min}^{-1}$ ), held at the same temperature for 24 h, and cooled to room temperature naturally. The resultant ingot was pulverized to obtain a powder. Iron(III) sulfate (50 mmol) was dissolved in distilled water (200 mL), and the  $\text{Bi}_2\text{Te}_3$  powder (12.7 g) was added. To this solution, a dispersion of pyrrole (0.495 g, 7.38 mmol) in distilled water (100 mL) was added with vigorous stirring. The resulting solution was stirred for 6 h to allow the chemical oxidation of the pyrrole by iron(III) sulfate, which was expected to result in the distribution of polypyrrole throughout the  $\text{Bi}_2\text{Te}_3$  powder. The solution was filtered and washed with deionized water and absolute ethanol. The resulting solid product was dried at 40 °C in a vacuum oven for 12 h, thus providing a mixed powder of  $\text{Bi}_2\text{Te}_3$  with polypyrrole. The mixed powder and the pristine  $\text{Bi}_2\text{Te}_3$  powder were packed using a spark plasma sintering instrument (Dr. Sinter, SPS3.20MK-IV). Approximately 12 g of each powder was separately placed into a cylindrical graphite mold (55 mm  $\times$  60 mm ( $d \times h$ )) with an inner hole of a 12 mm diameter for compaction at 350 and 400 °C for 2–3 min under a pressure of 100 MPa in an Ar atmosphere, providing cylindrical bulk specimens.

### 2.3. Characterizations

#### 2.3.1. Material Characterizations

X-ray diffraction (XRD) analysis was carried out using a D/MAX-2500 diffractometer (Rigaku, Tokyo, Japan) equipped with a scintillation counter detector. The XRD patterns were obtained in a  $2\theta$  range of 10–80°. Fourier-transform infrared (FTIR) spectra were obtained using a continuum spectrometer (iS50, Thermo Scientific, Waltham, MA, USA, spectral range:  $\leq 2000\text{ cm}^{-1}$ ). Raman spectra were recorded on a Nicolet spectrometer (Almea XR, Thermo Scientific, Waltham, MA, US, excitation photon energy: 532 nm), which can cover the spectral range of 100–2000  $\text{cm}^{-1}$ . Transmission electron microscopy (TEM) with selected-area electron diffraction (SAED) was conducted using a Titan G2 instrument (Titan G2 60-300, FEI Company, Hillsboro, OR, USA).

### 2.3.2. Thermoelectric Characterizations

The transport properties were measured for the faces of the sintered specimen that were vertical to the direction of the applied pressure. The carrier concentration ( $n$ ) was obtained using an HMS-3000 Hall effect measurement system (Ecopia). The electrical resistivity ( $\rho$ ) and Seebeck coefficient ( $\alpha$ ) were recorded in the temperature range of 25–200 °C using a ZEM-3 Seebeck/resistance measuring system (Ulvac-Rico). The carrier mobility ( $\mu$ ) was derived via the equation  $\mu = 1/(\rho ne)$ , where  $\rho$  is the electrical resistivity,  $n$  is the carrier concentration, and  $e$  is the elementary charge. The thermal conductivity ( $\kappa$ ) was calculated using the equation  $\kappa = \lambda C_p d$ , where  $\lambda$  is the thermal diffusivity,  $C_p$  is the specific heat, and  $d$  is the physical density. The thermal diffusivity ( $\lambda$ ) was recorded in the temperature range of 25–200 °C using a laser flash tool (LFA447, Netzsch, Selb, Germany). The specific heat was recorded using a differential scanning calorimeter (DSC200, Netzsch, Selb, Germany, Figure S1). The physical density ( $d$ ) was obtained via the Archimedes method (Table S1). The figure of merit was derived using the equation  $ZT = \alpha^2 \sigma T / \kappa$ . The thermal conductivity is roughly regarded as the sum of carrier ( $\kappa_c$ ) and lattice ( $\kappa_l$ ) thermal conductivities (i.e.,  $\kappa \approx \kappa_c + \kappa_l$ ). The carrier contribution was derived via the Wiedemann–Franz law  $\kappa_c = L_0 \sigma T$ , where  $L_0$  is the Lorenz number ( $2.0 \times 10^{-8} \text{ W}\Omega\text{K}^{-2}$  for a degenerate semiconductor) [23], and  $\sigma$  is the electrical conductivity. The lattice contribution was obtained by subtracting the carrier contribution from the overall thermal conductivity.

### 3. Results

In situ data of the spark plasma sintering (SPS) process for the powder samples were obtained to determine appropriate sintering conditions. We monitored a profile showing the variation in the Z-axis displacement of a cylindrical graphite mold filled with the powder samples during the SPS process (Figure 1). The sintering temperature was elevated by adjusting the electric current, resulting in a decrease in the Z-axis displacement, indicative of sample compaction.

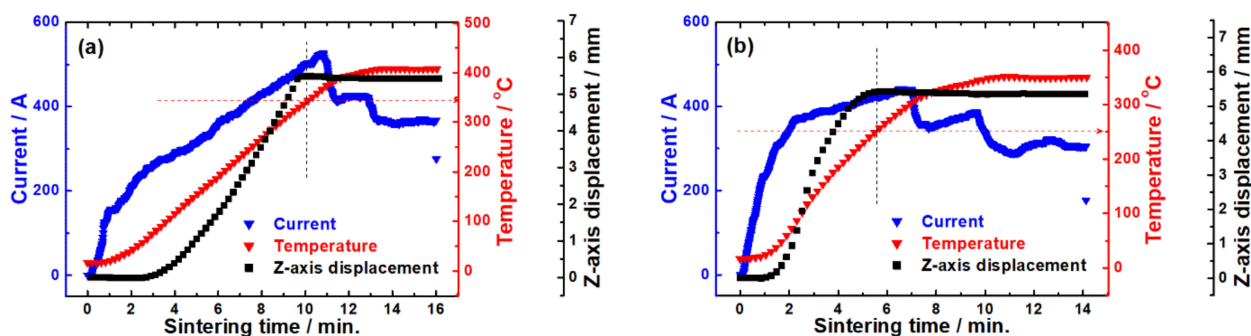


**Figure 1.** Variation in the Z-axis displacement of a graphite mold filled with (a) pristine  $\text{Bi}_2\text{Te}_3$  and (b)  $\text{Bi}_2\text{Te}_3$ -polypyrrole during the spark plasma sintering process at 400 and 350 °C, respectively, accompanied by the control of the electric current.

X-ray diffraction (XRD) patterns were obtained for the spark-plasma-sintered samples (Figure 2). Any noticeable change such as peak shift or new peak appearance was not detected in the diffraction patterns, although the sample was mixed with polypyrrole and/or was sintered at different temperatures.

Both FTIR and Raman spectroscopies were conducted to identify the inorganic and organic components in the samples, thus verifying whether the components were hybridized. These spectroscopies were also used to observe how the components' molecules were changed with the sintering temperature (Figure 3).

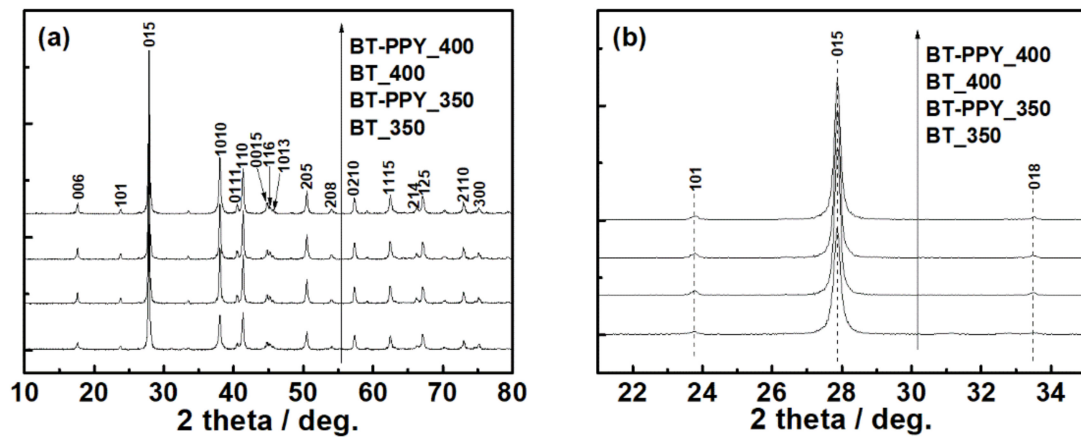


**Figure 2.** (a) XRD patterns of pristine  $\text{Bi}_2\text{Te}_3$  (BT) and  $\text{Bi}_2\text{Te}_3$ -polypyrrole (BT-PPY), which were individually sintered at 350 and 400 °C; (b) enlarged XRD plots of the BT and BT-PPY over a  $2\theta$  range from 21° to 35°.

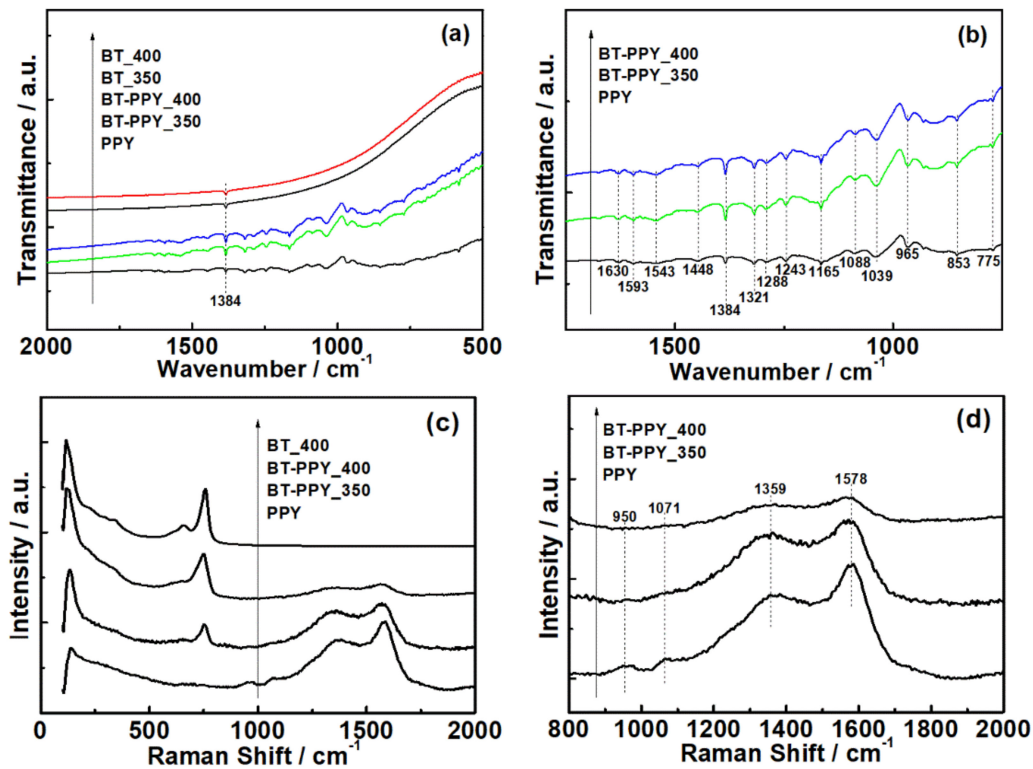


**Figure 3.** (a) FTIR spectra of pristine  $\text{Bi}_2\text{Te}_3$  (BT) and  $\text{Bi}_2\text{Te}_3$ -polypyrrole (BT-PPY), which were individually sintered at 350 and 400 °C, and polypyrrole (PPY); (b) enlarged FTIR spectra of BT-PPY and PPY in the wavenumber range from 750 to 1750  $\text{cm}^{-1}$ ; (c) Raman spectra of BT, BT-PPY, and PPY; (d) enlarged Raman spectra of BT-PPY and PPY in the range of Raman shift from 800 to 2000  $\text{cm}^{-1}$ .

TEM analyses were performed for the sintered samples to obtain information on morphology, crystallinity, and atomic arrangement of the inorganic and organic components. The information was used to confirm the unique interfaces between the components (Figure 4).

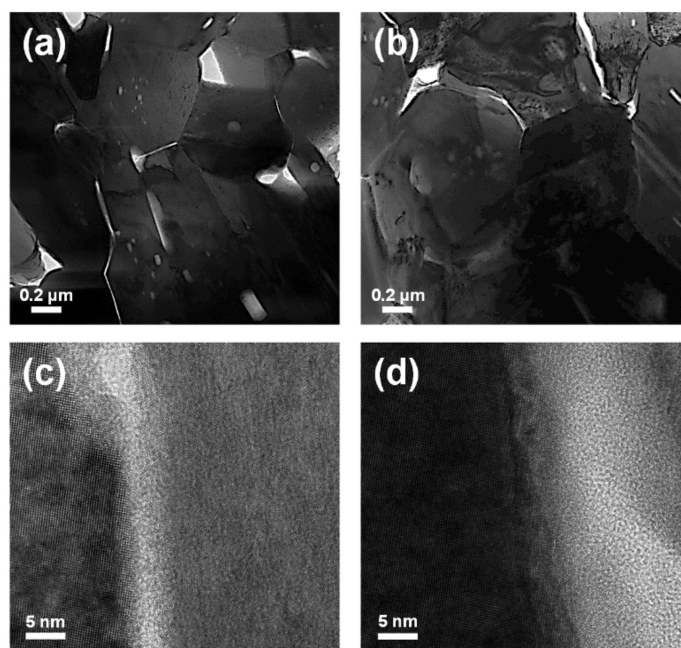


**Figure 4.** TEM images of the  $\text{Bi}_2\text{Te}_3$ -polypyrrole specimens sintered at 350 (a,c) and 400 °C (b,d) at different resolutions.

#### 4. Discussion

We preferentially monitored a profile showing the variation in the Z-axis displacement of a cylindrical graphite mold filled with pristine  $\text{Bi}_2\text{Te}_3$  during the SPS process (Figure 1a). As the sintering temperature was elevated by adjusting the electric current, the displacement increased because of sample compaction. When the sintering temperature reached around 350 °C, the displacement started to saturate, indicative of termination of the compaction. The sintering temperature kept increasing and then maintained at 400 °C for a few minutes to assure completion of the sintering. The resultant specimen of pristine  $\text{Bi}_2\text{Te}_3$  exhibited a relative density of over 98% compared to the theoretical density ( $7.86 \text{ g cm}^{-3}$ ) of  $\text{Bi}_2\text{Te}_3$  (Table S1, Supplementary Materials) [24]. A similar sintering strategy was applied to the mixed power of  $\text{Bi}_2\text{Te}_3$  and polypyrrole ( $\text{Bi}_2\text{Te}_3$ -polypyrrole). In  $\text{Bi}_2\text{Te}_3$ -polypyrrole, the Z-axis displacement began to saturate at a lower temperature by ca. 100 °C than in pristine  $\text{Bi}_2\text{Te}_3$  (Figure 1b) possibly due to the portion of polypyrrole having relatively poor temperature tolerance. To compare the pristine  $\text{Bi}_2\text{Te}_3$  specimen,  $\text{Bi}_2\text{Te}_3$ -polypyrrole was preferentially sintered at the same temperature (400 °C, Figure S2, Supplementary Materials). Considering that pristine  $\text{Bi}_2\text{Te}_3$  exhibited a saturated displacement from ca. 350 °C, we also attempted to sinter  $\text{Bi}_2\text{Te}_3$ -polypyrrole at 350 °C (Figure 1b). Both the  $\text{Bi}_2\text{Te}_3$ -polypyrrole specimens sintered at the two different temperatures recorded relatively low densities compared to the pristine  $\text{Bi}_2\text{Te}_3$  specimens (Table S1, Supplementary Materials) because of the portion of polypyrrole having much lower physical density (ca.  $1.4\text{--}1.5 \text{ g cm}^{-3}$ ) [25,26] than  $\text{Bi}_2\text{Te}_3$ .

The pristine  $\text{Bi}_2\text{Te}_3$  specimens exhibited an X-ray diffraction pattern of rhombohedral  $\text{Bi}_2\text{Te}_3$  (Figure 2a), identified as JCPDS Card No. 82-0358 (space group:  $R\bar{3}m (D_{3d}^5)$ ). The  $\text{Bi}_2\text{Te}_3$ -polypyrrole specimens displayed identical diffraction patterns to the pristine  $\text{Bi}_2\text{Te}_3$  specimens. Any diffraction pattern of polypyrrole was not observed in the  $\text{Bi}_2\text{Te}_3$ -polypyrrole specimens because polypyrrole exhibits only a broad diffraction peak, indicative of its typical amorphous nature (Figure S3, Supplementary Materials). According to the enlarged diffraction plot over a  $2\theta$  range of  $28^\circ$ , no considerable peak shifts were found in the strongest diffraction peaks for the (015) plane (Figure 2b). In addition, the specimens exhibited no significant differences in lattice parameters (Table S2, Supplementary Materials). These results possibly indicate that the addition of polypyrrole does not cause any lattice distortion of  $\text{Bi}_2\text{Te}_3$ . The FTIR spectra of pristine  $\text{Bi}_2\text{Te}_3$  and  $\text{Bi}_2\text{Te}_3$ -polypyrrole

are presented in Figure 3a. The spectra of pristine  $\text{Bi}_2\text{Te}_3$  showed nothing but the signal at  $1384\text{ cm}^{-1}$ , consistent with the characteristic signal of  $\text{Bi}_2\text{Te}_3$  [27]. This signal seemed to overlap with one of the polypyrrole peaks in the spectra of  $\text{Bi}_2\text{Te}_3$ -polypyrrole. The spectra of  $\text{Bi}_2\text{Te}_3$ -polypyrrole exhibited various characteristic signals for polypyrrole, such as C–C stretching vibration ( $775$ ,  $1088$ , and  $1165\text{ cm}^{-1}$ ), polypyrrole doping state ( $853$ ,  $965$ , and  $1384\text{ cm}^{-1}$ ), C–H out-of-plane bending vibration ( $1039\text{ cm}^{-1}$ ), N–H deforming vibration ( $1243\text{ cm}^{-1}$ ), C–N stretching vibration ( $1288\text{ cm}^{-1}$ ), C–H in-plane stretching vibration ( $1321\text{ cm}^{-1}$ ), C=C stretching vibration ( $1448$ ,  $1543$ , and  $1593\text{ cm}^{-1}$ ), and N–H in-plane bending vibration ( $1630\text{ cm}^{-1}$ ) (Figure 3b) [28,29].  $\text{Bi}_2\text{Te}_3$ -polypyrrole displayed most of the IR characteristic peaks of polypyrrole. This indicates that polypyrrole was not degraded despite the high sintering temperature of  $\text{Bi}_2\text{Te}_3$  ( $350$  or  $400\text{ }^\circ\text{C}$ ), but it retained the molecular structure possibly due to the short sintering time, thus being hybridized with  $\text{Bi}_2\text{Te}_3$ . Comparing the Raman spectra of the pristine  $\text{Bi}_2\text{Te}_3$  and  $\text{Bi}_2\text{Te}_3$ -polypyrrole specimens to that of polypyrrole, it was verified that the characteristic signals of  $\text{Bi}_2\text{Te}_3$  occurred below  $1000\text{ cm}^{-1}$ , while those for polypyrrole appeared above  $1000\text{ cm}^{-1}$  (Figure 3c). The spectrum of polypyrrole clearly displayed signals corresponding to C–C or C–N ring stretching mode and C=C stretching mode at  $1359$  and  $1578\text{ cm}^{-1}$ , respectively (Figure 3d) [30,31]. The spectrum of polypyrrole also showed peaks at  $950$  and  $1071\text{ cm}^{-1}$ , which are associated with bipolaron and polaron, respectively [30]. The presence of these peaks indicates that polypyrrole is highly oxidized. These peaks noticeably disappeared in  $\text{Bi}_2\text{Te}_3$ -polypyrrole sintered at  $350\text{ }^\circ\text{C}$  (Figure 3d). In addition,  $\text{Bi}_2\text{Te}_3$ -polypyrrole showed a somewhat decreased peak intensity for the stretching modes in the backbone chain (i.e., C–C or C–N and C=C stretching) compared to polypyrrole. In  $\text{Bi}_2\text{Te}_3$ -polypyrrole sintered at  $400\text{ }^\circ\text{C}$ , it was confirmed that the two satellite peaks were hardly detected, and the characteristic peaks for the stretching modes in the backbone chain were reduced even more. These results indicate that the original oxidation states in polypyrrole (i.e., bipolaron and polaron) were deformed, and even the polypyrrole molecule gradually degraded as the sintering temperature increased. It is expected that the  $\text{Bi}_2\text{Te}_3$ -polypyrrole specimens included fewer oxidized polypyrrole molecules having relatively short backbone chains compared to pristine polypyrrole. It inevitably occurred that the polypyrrole molecules were deformed or even degraded during the sintering process, but this molecular change was considered to possibly adjust by controlling the sintering temperature. The XRD, FTIR, and Raman results consistently indicate that  $\text{Bi}_2\text{Te}_3$ -polypyrrole exhibits both the characteristic signals of  $\text{Bi}_2\text{Te}_3$  and polypyrrole. It is expected that  $\text{Bi}_2\text{Te}_3$  is not chemically bonded to polypyrrole, but the former physically generates unique interfaces with the latter. To support this conclusion, we carried out TEM analyses for the  $\text{Bi}_2\text{Te}_3$ -polypyrrole specimens sintered at different temperatures (Figure 4). Both the specimens were mainly composed of irregularly shaped grains with a few micrometers in size (dark contrast). The specimens also contained bright-contrast grains, which were smaller than the dark-contrast grains and were not found in the pristine  $\text{Bi}_2\text{Te}_3$  specimens (Figure S4, Supplementary Materials). The dark grains in the  $\text{Bi}_2\text{Te}_3$ -polypyrrole specimens were found to have distinct crystalline directions, whereas the bright grains were observed to show an amorphous-looking phase (Figure 4). Periodic atomic arrangements were clearly observed in the dark grains, where the crystal directions of  $\text{Bi}_2\text{Te}_3$  were identified with a relevant SAED pattern (Figure 5a and inset). According to the SAED pattern with the zone axis along the  $[5\bar{5}1]$  direction, the dark grains were confirmed to have lattice fringes indexed as  $(015)$  and  $(10\bar{5})$  planes with interfaces of ca.  $3.2\text{ \AA}$ . No specific atomic arrangements were found for the bright grains (Figures 4 and 5), indicative of an amorphous phase of polypyrrole, and thus polypyrrole might have a diffraction peak that is too broad to appear in the  $\text{Bi}_2\text{Te}_3$ -polypyrrole specimens (Figure S3, Supplementary Materials). We confirmed that the  $\text{Bi}_2\text{Te}_3$  grains grew along different crystalline directions bordered by the grain boundaries with the amorphous phase of polypyrrole, resulting in the unique interfaces in the  $\text{Bi}_2\text{Te}_3$ -polypyrrole specimen (Figure 5b).

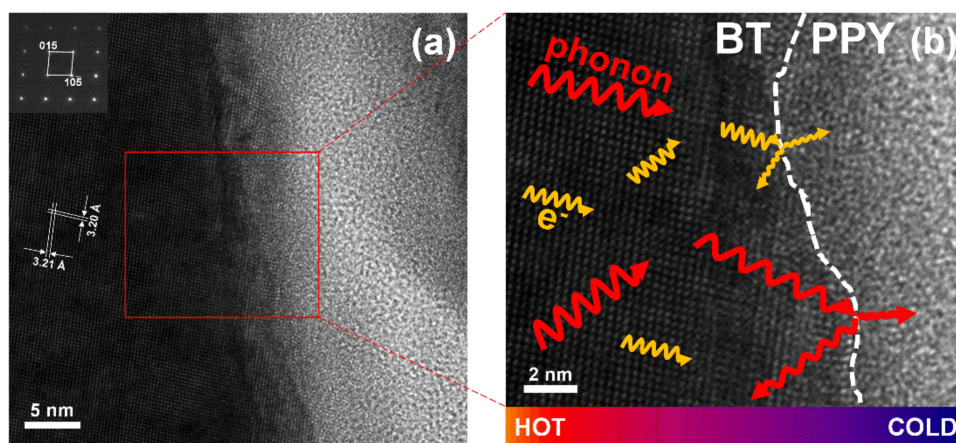


**Figure 5.** (a) TEM image of  $\text{Bi}_2\text{Te}_3$ -polypyrrole and the SAED pattern with the zone axis along the  $[\bar{5}\bar{5}1]$  direction (inlet) to identify the lattice fringes of  $\text{Bi}_2\text{Te}_3$ , (b) HR-TEM image of  $\text{Bi}_2\text{Te}_3$ -polypyrrole displaying the interface between  $\text{Bi}_2\text{Te}_3$  and polypyrrole components where electron and phonon scattering may occur.

Typical electrical conductivity of  $\text{Bi}_2\text{Te}_3$  (in the order of  $10^3 \text{ S cm}^{-1}$ ) [32,33] is much higher than that of polypyrrole (in the order of  $10^{-2}$ – $10^2 \text{ S cm}^{-1}$ ) [34,35] due to the predominant crystallinity of the former. Considering this great difference, it is easily comprehensible that electrical conductivity may decrease due to the polypyrrole addition to  $\text{Bi}_2\text{Te}_3$ .  $\text{Bi}_2\text{Te}_3$ -polypyrrole recorded higher electrical resistivity than pristine  $\text{Bi}_2\text{Te}_3$  up to 60% (Figure 6a). For this comparison, pristine  $\text{Bi}_2\text{Te}_3$  sintered at  $350^\circ\text{C}$  was used because it recorded better thermoelectric properties than that sintered at  $400^\circ\text{C}$ . The different thermoelectric properties of pristine  $\text{Bi}_2\text{Te}_3$  are elaborated in the Supplementary Materials (Figure S5).  $\text{Bi}_2\text{Te}_3$ -polypyrrole exhibited basically lower carrier concentration and mobility than pristine  $\text{Bi}_2\text{Te}_3$  (Table S3), and thus the former displayed higher electrical resistivity than the latter. In our previous work, we suggested the equilibrium band alignment with band-bending potential wells in the interface of  $\text{Bi}_2\text{Te}_3$  and polypyrrole by using their energy band structures [22]. Because of the band bending, the accumulation of electrons and holes possibly occurs at the interfaces, thereby causing the carrier offsetting, which explains the decrease in the carrier concentration in  $\text{Bi}_2\text{Te}_3$ -polypyrrole. Carrier transport may be interrupted by the interfaces between the  $\text{Bi}_2\text{Te}_3$  and polypyrrole components (Figure 5b) and by the reduced physical densities (Table S1), resulting in the decrease in carrier mobility of  $\text{Bi}_2\text{Te}_3$ -polypyrrole. As the sintering temperature increased,  $\text{Bi}_2\text{Te}_3$ -polypyrrole exhibited increases both in the carrier concentration and mobility (Table S3). Because of both increases,  $\text{Bi}_2\text{Te}_3$ -polypyrrole sintered at  $400^\circ\text{C}$  recorded lower electrical resistivity than that sintered at  $350^\circ\text{C}$  (Figure 6a). As verified in the Raman spectroscopy results (Figure 3d), the original oxidation states in polypyrrole (i.e., bipolaron and polaron) were deformed, and even polypyrrole degradation was accelerated as the sintering temperature increased; thus,  $\text{Bi}_2\text{Te}_3$ -polypyrrole sintered at  $400^\circ\text{C}$  might have exhibited a higher carrier concentration and mobility than that sintered at  $350^\circ\text{C}$ . As explained above (Table S3), the carrier concentration decreased due to the addition of polypyrrole, and thus  $\text{Bi}_2\text{Te}_3$ -polypyrrole exhibited a higher Seebeck coefficient than pristine  $\text{Bi}_2\text{Te}_3$  up to 33% (Figure 6b). When the sintering temperature increased,  $\text{Bi}_2\text{Te}_3$ -polypyrrole showed an increase in the carrier concentration as confirmed above, thus providing decreases in both electrical resistivity and the Seebeck coefficient (Figure 6a,b). Consequently,  $\text{Bi}_2\text{Te}_3$ -polypyrrole recorded a higher power factor than pristine  $\text{Bi}_2\text{Te}_3$  up to 14%, whereas  $\text{Bi}_2\text{Te}_3$ -polypyrrole displayed no significant change in the power factor depending on the sintering temperature (Figure 6c).

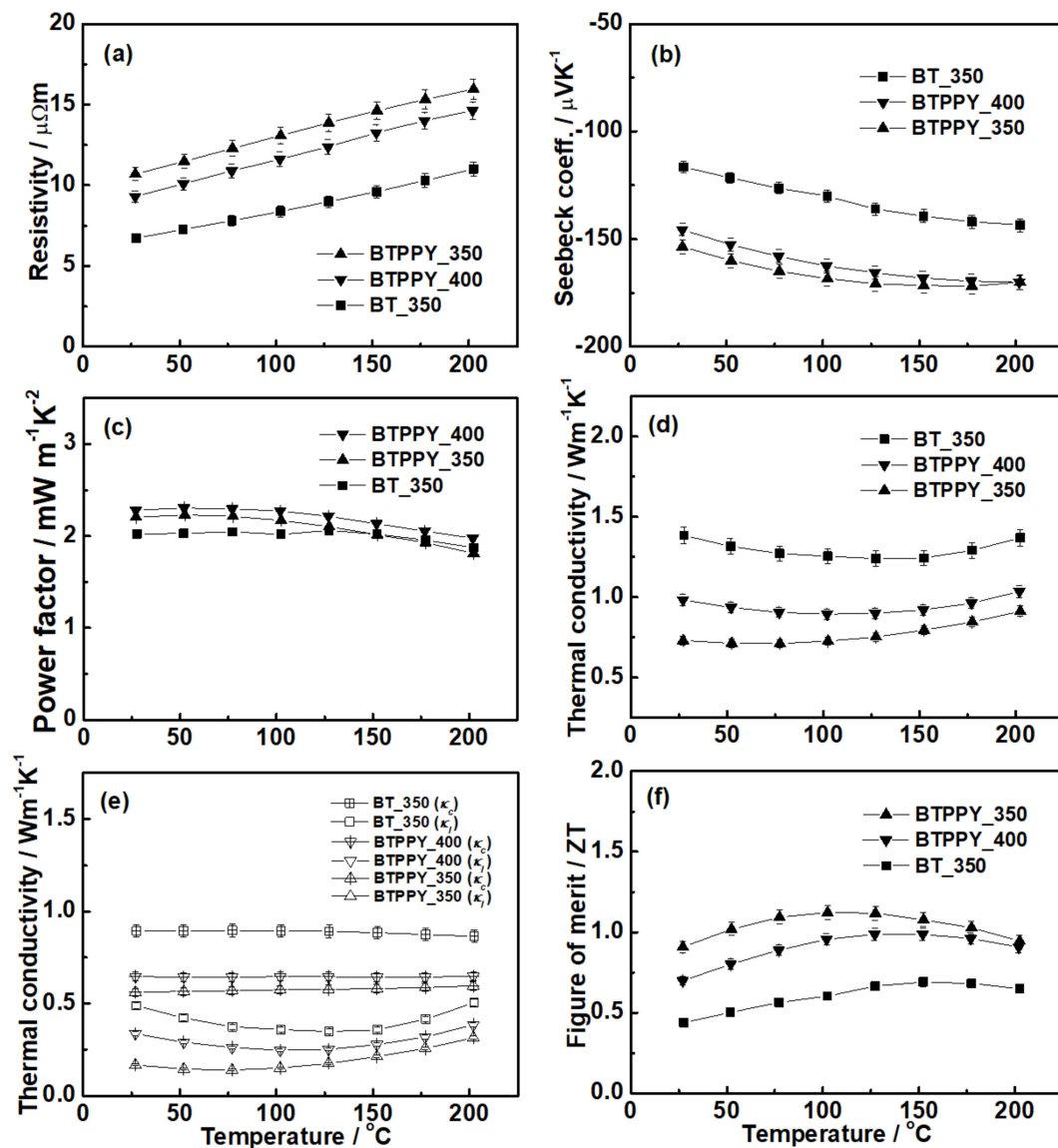


**Figure 6.** Thermoelectric properties of the pristine Bi<sub>2</sub>Te<sub>3</sub> and Bi<sub>2</sub>Te<sub>3</sub>-polypyrrole specimens sintered at 350 and 400 °C: (a) electrical resistivity, (b) Seebeck coefficient, (c) power factor, (d) thermal conductivity divided into (e) carrier ( $\kappa_c$ ) and lattice ( $\kappa_l$ ) contributions, and (f) ZT. Error bars are shown when they exceed the symbol size.

Bi<sub>2</sub>Te<sub>3</sub>-polypyrrole exhibited lower thermal conductivity than pristine Bi<sub>2</sub>Te<sub>3</sub> up to 50% because the former had lower carrier and lattice thermal conductivities than the latter (Figure 6d,e). Both the carrier concentration and mobility decreased due to the addition of polypyrrole, and thus Bi<sub>2</sub>Te<sub>3</sub>-polypyrrole showed decreased carrier thermal conductivity. In addition, Bi<sub>2</sub>Te<sub>3</sub>-polypyrrole may possess vigorous phonon scattering at the interfaces of Bi<sub>2</sub>Te<sub>3</sub> and polypyrrole components (Figure 5b), thus providing decreased lattice thermal conductivity. However, the thermal conductivity of Bi<sub>2</sub>Te<sub>3</sub>-polypyrrole increased as the sintering temperature elevated because of the increased carrier and lattice thermal contributions (Figure 6e). The degradation of polypyrrole was accelerated due to the increased sintering temperature, and thus Bi<sub>2</sub>Te<sub>3</sub>-polypyrrole exhibited an increased carrier concentration and mobility and a decreased amount of interface for phonon scattering, resulting in the increased carrier and lattice thermal contributions, respectively.

By introducing polypyrrole to Bi<sub>2</sub>Te<sub>3</sub> and adjusting the compaction conditions of the resulting materials, the inorganic/organic composite (Bi<sub>2</sub>Te<sub>3</sub>-polypyrrole) in the bulk phase was successfully developed. By adequately adding the organic component, the

electrical property was somewhat increased, while the thermal conductivity was significantly reduced; thus, remarkable ZT enhancement was accomplished (Figure 6f). Bi<sub>2</sub>Te<sub>3</sub>-polypyrrole recorded ZT maximum (ZT<sub>max</sub>) and average (ZT<sub>ave</sub>) values of 1.18 at 100 °C and 1.12 at 50–150 °C, which were approximately twice as what pristine Bi<sub>2</sub>Te<sub>3</sub> exhibited. These ZT values are not only superior to those previously reported as the highest performance for n-type binary Bi<sub>2</sub>Te<sub>3</sub>, but they are also as competent as the excellent performance of n-type ternary Bi<sub>2</sub>(Te,Se)<sub>3</sub> recently reported (Table S4, Supplementary Materials) [36–38].

## 5. Conclusions

Bi<sub>2</sub>Te<sub>3</sub> was hybridized with polypyrrole to produce a bulk composite (Bi<sub>2</sub>Te<sub>3</sub>-polypyrrole) including the interface, where the effects of energy band junction and phonon scattering effects possibly occur. The effects may cause noticeable changes in thermoelectric transport properties, as presented below.

1. The composite exhibited a decrease in the carrier concentration, possibly due to carrier offsetting at the interface consisting of the energy band junction. The composite showed a slight increase in the power factor compared to pristine Bi<sub>2</sub>Te<sub>3</sub> because of the decrease in the carrier concentration.
2. The composite recorded lower thermal conductivity than pristine Bi<sub>2</sub>Te<sub>3</sub> because the former exhibited lower carrier and lattice thermal conductivities, which resulted from the decrease in the carrier concentration and the phonon scattering effect at the interface, respectively.
3. The decoupling effect of the electrical and thermal properties resulted in remarkably enhanced ZT values, which may be evaluated as the highest performance among n-type binary Bi<sub>2</sub>Te<sub>3</sub>. Because of the superior ZT values at low temperatures, the composite may be highly applicable to thermoelectric operations at low temperatures, such as energy-harvesting devices and systems.

We are currently conducting further studies on the interaction mechanism and theory and various compositions between the components.

**Supplementary Materials:** The following are available online at <https://www.mdpi.com/article/10.3390/ma14113080/s1>, Figure S1: Specific heat (Cp), Figure S2: In situ data of the spark plasma sintering process, Figure S3: X-ray diffraction (XRD) data, Figure S4: Transmission electron microscopy (TEM), Figure S5: Thermoelectric properties, Table S1: Physical density data, Table S2: Lattice parameters, Table S3: Carrier concentration and mobility, Table S4: ZT values.

**Author Contributions:** Conceptualization, C.K.; methodology, C.K.; validation, C.K. and D.H.L.; formal analysis, C.K.; investigation, C.K.; resources, C.K.; writing—original draft preparation, C.K.; writing—review and editing, C.K. and D.H.L.; visualization, C.K.; funding acquisition, C.K. All authors have read and agreed to the published version of the manuscript.

**Funding:** This research was funded by the DGIST R&D Program of the Ministry of Science, ICT, and Technology of Korea, Grant Number 21-ET-07. This work was also supported by the National Research Foundation of Korea (NRF) grant funded by the Korean government (MSIT) (No. 2021R1F1A1045583).

**Institutional Review Board Statement:** Not applicable.

**Informed Consent Statement:** Not applicable.

**Data Availability Statement:** The data presented in this study are available on request from the corresponding author.

**Conflicts of Interest:** The authors declare no conflict of interest.

## References

1. Dresselhaus, M.S.; Chen, G.; Tang, M.Y.; Yang, R.G.; Lee, H.; Wang, D.Z.; Ren, Z.F.; Fleurial, J.-P.; Gogna, P. New Directions for Low-Dimensional Thermoelectric Materials. *Adv. Mater.* **2007**, *19*, 1043–1053. [CrossRef]
2. Hsu, K.F.; Loo, S.; Guo, F.; Chen, W.; Dyck, J.S.; Uher, C.; Hogan, T.; Polychroniadis, E.K.; Kanatzidis, M.G. Cubic AgPbmS-bTe<sub>2+m</sub>: Bulk Thermoelectric Materials with High Figure of Merit. *Science* **2004**, *303*, 818–821. [CrossRef] [PubMed]

3. He, J.; Tritt, T.M. Advances in thermoelectric materials research: Looking back and moving forward. *Science* **2017**, *357*, eaak9997. [[CrossRef](#)] [[PubMed](#)]
4. Goldsmid, H.J. *Introduction to Thermoelectricity*; Springer: Berlin, Germany, 2009; pp. 72–77. [[CrossRef](#)]
5. Rowe, D.M. *Thermoelectrics Handbook: Macro to Nano*; CRC/Taylor & Francis: Boca Raton, FL, USA, 2006; pp. 1–10. Available online: <https://www.routledge.com/Thermoelectrics-Handbook-Macro-to-Nano/Rowe/p/book/9780849322648> (accessed on 6 March 2021).
6. Ji, X.; Zhang, B.; Tritt, T.M.; Kolis, J.W.; Kumbhar, A. Solution-Chemical Syntheses of Nano-Structured Bi<sub>2</sub>Te<sub>3</sub> and PbTe Thermoelectric Materials. *J. Electron. Mater.* **2007**, *36*, 721–726. [[CrossRef](#)]
7. Takabatake, T. *Thermoelectric Nanomaterials: Materials Design and Applications*; Koumoto, K., Mori, T., Eds.; Springer: Berlin, Germany, 2009; pp. 33–49. [[CrossRef](#)]
8. Chen, Z.-G.; Han, G.; Yang, L.; Cheng, L.; Zou, J. Nanostructured thermoelectric materials: Current research and future challenge. *Prog. Nat. Sci.* **2012**, *22*, 535–549. [[CrossRef](#)]
9. Ortega, S.; Ibáñez, M.; Liu, Y.; Zhang, Y.; Kovalenko, M.V.; Cadavid, D.; Cabot, A. Bottom-up engineering of thermoelectric nanomaterials and devices from solution-processed nanoparticle building blocks. *Chem. Soc. Rev.* **2017**, *46*, 3510–3528. [[CrossRef](#)]
10. Ghosh, S.; Valiyaveetil, S.M.; Shankar, G.; Maity, T.; Chen, K.-H.; Biswas, K.; Suwas, S.; Mallik, R.C. Enhanced Thermoelectric Properties of In-Filled Co<sub>4</sub>Sb<sub>12</sub> with InSb Nanoinclusions. *ACS Appl. Energy Mater.* **2019**, *3*, 635–646. [[CrossRef](#)]
11. Yazdani, S.; Pettes, M.T. Nanoscale self-assembly of thermoelectric materials: A review of chemistry-based approaches. *Nanotechnology* **2018**, *29*, 432001. [[CrossRef](#)]
12. Li, G.; Yang, J.; Xiao, Y.; Fu, L.; Luo, Y.; Zhang, D.; Liu, M.; Li, W.; Zhang, M. Effect of TiC Nanoinclusions on Thermoelectric and Mechanical Performance of Polycrystalline In<sub>4</sub>Se<sub>2.65</sub>. *J. Am. Ceram. Soc.* **2015**, *98*, 3813–3817. [[CrossRef](#)]
13. Zhang, B.; Sun, J.; Katz, H.E.; Fang, F.; Opila, R.L. Promising Thermoelectric Properties of Commercial PEDOT:PSS Materials and Their Bi<sub>2</sub>Te<sub>3</sub> Powder Composites. *ACS Appl. Mater. Interfaces* **2010**, *2*, 3170–3178. [[CrossRef](#)]
14. Kim, C.; Yang, Y.; Baek, J.Y.; Lopez, D.H.; Kim, D.H.; Kim, H. Concurrent defects of intrinsic tellurium and extrinsic silver in an n-type Bi<sub>2</sub>Te<sub>2.88</sub>Se<sub>0.15</sub> thermoelectric material. *Nano Energy* **2019**, *60*, 26–35. [[CrossRef](#)]
15. Kim, C.; Lopez, D.H.; Kim, D.H.; Kim, H. Dual defect system of tellurium antisites and silver interstitials in off-stoichiometric Bi<sub>2</sub>(Te,Se)<sub>3+y</sub> causing enhanced thermoelectric performance. *J. Mater. Chem. A* **2018**, *7*, 791–800. [[CrossRef](#)]
16. Xu, S.; Hong, M.; Shi, X.-L.; Wang, Y.; Ge, L.; Bai, Y.; Wang, L.; Dargusch, M.; Zou, J.; Chen, Z.-G. High-Performance PEDOT:PSS Flexible Thermoelectric Materials and Their Devices by Triple Post-Treatments. *Chem. Mater.* **2019**, *31*, 5238–5244. [[CrossRef](#)]
17. Fan, Z.; Ouyang, J. Thermoelectric Properties of PEDOT:PSS. *Adv. Electron. Mater.* **2019**, *5*, 1800769-1–1800769-23. [[CrossRef](#)]
18. Bharti, M.; Singh, A.; Samanta, S.; Aswal, D. Conductive polymers for thermoelectric power generation. *Prog. Mater. Sci.* **2018**, *93*, 270–310. [[CrossRef](#)]
19. Yusupov, K.; Vomiero, A. Polymer-Based Low-Temperature Thermoelectric Composites. *Adv. Funct. Mater.* **2020**, *30*, 2002015-1–2002015-26. [[CrossRef](#)]
20. Thongkham, W.; Lertsatitthanakorn, C.; Jiramitmongkon, K.; Tantisantisom, K.; Boonkoom, T.; Jitpukdee, M.; Sinthiptharakoon, K.; Klamchuen, A.; Liangruksa, M.; Khanchaitit, P. Self-Assembled Three-Dimensional Bi<sub>2</sub>Te<sub>3</sub> Nanowire–PEDOT:PSS Hybrid Nanofilm Network for Ubiquitous Thermoelectrics. *ACS Appl. Mater. Interfaces* **2019**, *11*, 6624–6633. [[CrossRef](#)]
21. Bae, E.J.; Kang, Y.H.; Jang, K.-S.; Lee, C.; Cho, S.Y. Solution synthesis of telluride-based nano-barbell structures coated with PEDOT:PSS for spray-printed thermoelectric generators. *Nanoscale* **2016**, *8*, 10885–10890. [[CrossRef](#)]
22. Kim, C.; Baek, J.Y.; Lopez, D.H.; Kim, D.H.; Kim, H. Decoupling effect of electrical and thermal properties of Bi<sub>2</sub>Te<sub>3</sub>-polypyrrole hybrid material causing remarkable enhancement in thermoelectric performance. *J. Ind. Eng. Chem.* **2019**, *71*, 119–126. [[CrossRef](#)]
23. Sales, B.C.; Mandrus, D.; Chakoumakos, B.C.; Keppens, V.; Thompson, J.R. Filled Skutterudite Antimonides: Electron Crystals and Phonon Glasses. *Phys. Rev. B* **1997**, *56*, 15081–15089. [[CrossRef](#)]
24. Yu, F.; Zhang, J.; Yu, D.; He, J.; Liu, Z.; Xu, B.; Tian, Y. Enhanced thermoelectric figure of merit in nanocrystalline Bi<sub>2</sub>Te<sub>3</sub> bulk. *J. Appl. Phys.* **2009**, *105*, 094303. [[CrossRef](#)]
25. Qi, Z.; Pickup, P.G. Size Control of Polypyrrole Particles. *Chem. Mater.* **1997**, *9*, 2934–2939. [[CrossRef](#)]
26. Lei, J.; Cai, Z.; Martin, C.R. Effect of reagent concentrations used to synthesize polypyrrole on the chemical characteristics and optical and electronic properties of the resulting polymer. *Synth. Met.* **1992**, *46*, 53–69. [[CrossRef](#)]
27. Jiang, Q.; Liu, C.; Song, H.; Xu, J.; Mo, D.; Shi, H.; Wang, Z.; Jiang, F.; Lu, B.; Zhu, Z. Free-standing PEDOT:PSS Film as Electrode for the Electrodeposition of Bismuth Telluride and Its Thermoelectric Performance. *Int. J. Electrochem. Sci.* **2014**, *9*, 7540–7551.
28. Dallas, P.; Niarchos, D.; Vrbancic, D.; Boukos, N.; Pejovnik, S.; Trapalis, C.; Petridis, D. Interfacial polymerization of pyrrole and in situ synthesis of polypyrrole/silver nanocomposites. *Polymer* **2007**, *48*, 2007–2013. [[CrossRef](#)]
29. Jia, Y.; Xiao, P.; He, H.; Yao, J.; Liu, F.; Wang, Z.; Li, Y. Photoelectrochemical properties of polypyrrole/TiO<sub>2</sub> nanotube arrays nanocomposite under visible light. *Appl. Surf. Sci.* **2012**, *258*, 6627–6631. [[CrossRef](#)]
30. Singh, A.; Salmi, Z.; Jha, P.; Joshi, N.; Kumar, A.; Decorse, P.; Lecoq, H.; Lau-Truong, S.; Aswal, D.K.; Gupta, S.K.; et al. One step synthesis of highly ordered free standing flexible polypyrrole-silver nanocomposite films at air–water interface by photopolymerization. *RSC Adv.* **2013**, *3*, 13329–13336. [[CrossRef](#)]
31. Gu, Z.; Li, C.; Wang, G.; Zhang, L.; Li, X.; Wang, W.; Jin, S. Synthesis and characterization of polypyrrole/graphite oxide composite by in situ emulsion polymerization. *J. Polym. Sci. Part B Polym. Phys.* **2010**, *48*, 1329–1335. [[CrossRef](#)]

32. Han, M.-K.; Sung-Jin, K.; Lee, D.-H.; Kim, S.-J. Thermoelectric Properties of Bi<sub>2</sub>Te<sub>3</sub>: CuI and the Effect of Its Doping with Pb Atoms. *Materials* **2017**, *10*, 1235. [[CrossRef](#)]
33. Carroll, E.; Buckley, D.; Mogili, N.V.V.; McNulty, D.; Moreno, M.S.; Glynn, C.; Collins, G.; Holmes, J.D.; Razeeb, K.M.; O'Dwyer, C. 2D Nanosheet Paint from Solvent-Exfoliated Bi<sub>2</sub>Te<sub>3</sub> Ink. *Chem. Mater.* **2017**, *29*, 7390–7400. [[CrossRef](#)]
34. Mathys, G.; Truong, V.-T. Spectroscopic study of thermo-oxidative degradation of polypyrrole powder by FT-IR. *Synth. Met.* **1997**, *89*, 103–109. [[CrossRef](#)]
35. Sak-Bosnar, M.; Budimir, M.V.; Kovac, S.; Kukulj, D.; Duic, L. Chemical and electrochemical characterization of chemically synthesized conducting polypyrrole. *J. Polym. Sci. Part A Polym. Chem.* **1992**, *30*, 1609–1614. [[CrossRef](#)]
36. Wu, F.; Song, H.; Gao, F.; Shi, W.; Jia, J.; Hu, X. Effects of Different Morphologies of Bi<sub>2</sub>Te<sub>3</sub> Nanopowders on Thermoelectric Properties. *J. Electron. Mater.* **2013**, *42*, 1140–1145. [[CrossRef](#)]
37. Xu, B.; Feng, T.; Agne, M.T.; Zhou, L.; Ruan, X.; Snyder, G.J.; Wu, Y. Highly Porous Thermoelectric Nanocomposites with Low Thermal Conductivity and High Figure of Merit from Large-Scale Solution-Synthesized Bi<sub>2</sub>Te<sub>2.5</sub>Se<sub>0.5</sub> Hollow Nanostructures. *Angew. Chem. Int. Ed.* **2017**, *56*, 3546–3551. [[CrossRef](#)]
38. Hong, M.; Chasapis, T.C.; Chen, Z.-G.; Yang, L.; Kanatzidis, M.G.; Snyder, G.J.; Zou, J. n-Type Bi<sub>2</sub>Te<sub>3</sub>-xSex Nanoplates with Enhanced Thermoelectric Efficiency Driven by Wide-Frequency Phonon Scatterings and Synergistic Carrier Scatterings. *ACS Nano* **2016**, *10*, 4719–4727. [[CrossRef](#)]